High Fill Factor and Reduced Hysteresis Perovskite Solar Cells Using Small-Molecule-Engineered Nickel Oxide as the Hole Transport Layer

Yuze Li, Jia-Jiu Ye, Asma Medjahed, Dmitry Aldakov, Stéphanie Pouget, Elisabeth Djurado, Lin Xu, Peter Reiss

High Fill Factor and Reduced Hysteresis Perovskite Solar Cells Using Small Molecule-Engineered Nickel Oxide as Hole Transport Layer

Yuze Li,[1] Jia-Jiu Ye,[1,#] Asma Medjahed,[1] Dmitry Aldakov,[1] Stéphanie Pouget,[2] Elisabeth Djurado,[3] Lin Xu,[4,*] Peter Reiss[1,*]

[1]*Univ. Grenoble Alpes, CEA, CNRS, INP, IRIG/SyMMES, STEP, 38000 Grenoble, France*
[2]*Univ. Grenoble Alpes, CEA, IRIG/MEM, SGX, 38000 Grenoble, France*
[3]*Univ. Grenoble Alpes, Univ. Savoie Mont Blanc, CNRS, Grenoble INP, LEPMI, 38000 Grenoble, France*
[4]*State Key Laboratory on Integrated Optoelectronics, College of Electronic Science and Engineering, Jilin University, 2699 Qianjin Street, Changchun 130012, China*

* Email: linxu@jlu.edu.cn, peter.reiss@cea.fr

Abstract:

Nickel oxide (NiO_x) is an emerging hole transport layer (HTL) material in halide perovskite solar cells (PSCs), combining high hole mobility, transparency, and stability. Current limitations of the device performance are mainly related to the inefficient hole extraction caused by contact problems between NiO_x and the perovskite layer. Based on its expected strong interaction with both the NiO_x surface and the perovskite layer, we selected 4-dimethylaminopyridine (DMAP) as a molecular passivation agent for the HTL. Photoelectron spectroscopy and photophysical studies demonstrate that DMAP passivation creates a more favorable band alignment at the NiO_x/perovskite interface. This leads to decreased carrier recombination near the interface and to enhanced hole transfer. In addition, X-ray diffraction reveals reduced strain, improved crystalline quality, and a redistribution of excess PbI_2 in perovskite layers grown on DMAP-passivated NiO_x. As a consequence, PSCs with the DMAP-modified HTL exhibit a strongly increased fill factor and power conversion efficiency with values close to 80% and 18%, respectively. Moreover, they show negligible hysteresis and enhanced environmental stability compared to devices with untreated HTLs.

Keywords: NiO, hole transport layer, perovskite solar cells, fill factor, 4-dimethylaminopyridine

1. Introduction

Organic-inorganic lead halide perovskite solar cells (PSCs) constitute an emerging family of photovoltaic devices, which benefit from the highly advantageous features of the perovskite active material such as efficient light absorption,[1] long charge carriers diffusion length,[2] and low fabrication cost. With a power conversion efficiency (PCE) of more than 25% (25.7% certified) achieved in only 12 years of development, they are one of the most promising upcoming photovoltaic technologies.[3,4] The ambipolar character of halide perovskite materials enables a variety of device designs, encompassing mesoscopic and planar devices with *n–i–p* or *p–i–n* architectures. The more widely studied *n-i-p* structures, in which metal oxides (TiO_2, SnO_2, ZnO, etc.) and spiro-OMeTAD (N^2,N^2,$N^{2'}$,$N^{2'}$,N^7,N^7,$N^{7'}$,$N^{7'}$-octakis(4-methoxyphenyl)-9,9′-spirobi[9H-fluorene]-2,2′,7,7′-tetramine) are commonly used as electron transport layer (ETL) and hole transport layer (HTL), respectively,[3] are prone to hysteresis effects when measuring the *J*/*V* curves, making it difficult to properly assess the PCE.[5] This phenomenon is commonly attributed to unbalanced charge transport and accumulation of carriers near the interfaces due to a large defect density near the perovskite surface,[6] interstitial excess ions screening effects,[7] or ferroelectric properties.[8] The *p-i-n* architecture is an appealing alternative as it provides negligible hysteresis effects and the possibility of simpler and low-temperature fabrication processes, making it also highly suitable for use in tandem solar cells.[9]

Among inverted structure PSCs, poly(3,4-ethylenedioxythiophene) polystyrene sulfonate (PEDOT:PSS) and poly[bis(4-phenyl)(2,4,6-trimethylphenyl)amine] (PTAA) are commonly used HTLs, [10–12] with a highest certified PCE of 24.3%.[13] However, electrode corrosion caused by the acidity of PEDOT:PSS causes reduced operational stability, and the interest in PTAA for use in scalable PSCs is limited due to its high cost. Nickel oxide (NiO_x) has recently sparked a significant interest as a potential candidate for inorganic HTLs. NiO_x possesses an appropriate bandgap (around 3.5 eV) as well as a deep-lying valence band maximum (VBM: 5.0-5.2eV),[14,15] both beneficial for a suitable band alignment with lead halide perovskites. Moreover, the inexpensive and facile preparation processes of NiO_x-based HTLs enable a straightforward scale-up for industrial production. Several approaches for preparing NiO_x HTLs have been reported, such as solution-based processes,[16] pulsed laser deposition,[17] and the sol-gel technique.[18] In parallel, different types of dopants have been explored to improve the conductivity of NiO_x, such as Cu, Mg and Li.[19] As an example, Li and coworkers developed Mg-doped NiO_x HTLs of enhanced conductivity leading to a maximum PCE of 18.2% for small-area devices and 15.3% for 1 cm^2

devices.[20] To further improve the hole-extraction capability of the NiO_x layer, Ru et al. synthesized molecular TCNQ (7,7,8,8-tetracyanoquinodimethane) derivatives of controlled electron affinity to dope the precursor solution of NiO_x nanoparticles. The resulting HTLs showed a marked conductivity improvement and a decreased energy gap, yielding a promising PCE of PSCs (22.13%).[21]

Although the PCEs of PSCs based on NiO_x HTLs have been largely improved, there is still a gap when compared with the performance of solar cells in *n-i-p* configuration, with the major limitations being the fill factor (*FF*) and short-circuit current density (J_{sc}). The lower crystalline quality of the perovskite grown on NiO_x and the poor contact, caused by surface defects of NiO_x, have been identified as the main limiting factors.[22] Surface modification is an effective way to passivate the NiO_x layer, improving the interfacial contact and adjusting the energy levels, which can lead to a better hole extraction and thereby enhance the *FF* and J_{sc}.[19] In contrast to the large choice of passivation layers reported for *n-i-p* PSCs, much fewer works concern NiO_x in *p-i-n* configuration. As typical examples diethanolamine (DEA) and ferrocenedicarboxylic acid (FDA) have been proposed, interacting via the amine or the carboxylic acid function with the NiO_x surface, respectively.[22,23] In another example, by bridging the NiO_x nanocrystalline film with the perovskite layer via a self-assembled monolayer consisting of two types of molecules comprising carbazole and phosphonic acid groups, interfacial recombination was mitigated and hole extraction improved, resulting in an efficiency of 24.7% for flexible all-perovskite tandem solar cells.[24] Further examples of NiO_X functionalization have been summarized in recent reviews.[25,26]

In this work, we explore 4-dimethylaminopyridine (DMAP), a bifunctional molecule assuring strong interaction with both the HTL and the perovskite layer, as the passivation agent for sol-gel processed NiO_x HTLs. To enhance the conductivity of NiO_x, 5 mol% of Cu dopant is used,[27] and the resulting HTL is therefore referred to as Cu:NiO_x. DMAP preferentially binds to undercoordinated Ni cations at the HTL surface via its pyridine nitrogen, due to its high nucleophilicity.[28] Upon deposition of the perovskite layer on DMAP-passivated Cu:NiO_x, the remaining dimethylamino moiety can efficiently interact with lead ions. Therefore, DMAP can passivate defects at the HTL-perovskite interface and act at the same time as a nucleation center for the perovskite layer. Our results demonstrate that the treatment of the HTL with DMAP not only improves the perovskite crystalline quality but also leads to a more favorable energy level alignment at the HTL/perovskite interface, facilitating hole extraction. As a consequence, planar *p-i-n* PSCs with DMAP-passivated NiO_x present significantly improved

performances compared to identical devices without DMAP, reaching *FF* and *PCE* values of almost 80% and 18%, respectively, and showing strongly reduced hysteresis. Moreover, enhanced environmental stability of the solar cells is observed when exposing them to ambient air with 50% humidity.

2. Results and Discussion

In the DMAP molecule, electron donation from the dimethylamino group into the aromatic ring and resonance stabilization lead to high basicity of the pyridine nitrogen. Therefore, as illustrated in **Fig. 1A**, DMAP is expected to coordinate with the NiO_x film surface via its pyridine nitrogen. The dimethylamino group, on the other hand, is available for coordinating Pb ions of the perovskite layer via the electron lone pair of its nitrogen atom. To probe this interaction, DMAP and PbI_2 were mixed and annealed at 150° C for 5 min. A new compound formed, as indicated by the color change from yellow (PbI_2) to white (cf. **Fig. S1**). **Fig. 1B** presents the Fourier-transform infrared (FTIR) spectra of DMAP and the new complex. Because of the coordination of the dimethylamino group to the Pb center, the spectrum of DMAP-PbI_2 shows a clear change in the signals related to the symmetric and asymmetric stretching vibrations of the C-H bonds of the methyl groups in the range of 3000-2800 cm^{-1} (indicated by the dashed line). Furthermore, the amine C-N bond stretching vibration (ν(C–N)) shifts from 1373 cm^{-1} (DMAP) to 1381 cm^{-1} (DMAP-PbI_2).[29] To further check the chemical state of the N atom in the complex, X-ray photoelectron spectroscopy (XPS) was performed (**Fig. S2**). XPS cannot distinguish between the pyridine and amine nitrogen atoms in DMAP. Nonetheless, the N1s spectrum displays a shift to lower energy (-0.16 eV) after coordination with PbI_2 signaling a weak reduction of the nitrogen atom due to the interaction between PbI_2 and DMAP.

In the one-step perovskite deposition process from solutions comprising methylammonium iodide (MAI) and PbI_2, the perovskite precursor solution contains iodoplumbate intermediates (PbI_n^{2-n}, n = 2-6) and lead–solvent complexes.[30,31] The presence and concentration of these compounds subsequently determine the defect density and morphology of the fully formed perovskite active layer.[32] We expect that DMAP favors the assembly of iodoplumbates on the NiO_x surface, leading to nucleation centers for the perovskite layer. The interaction between the DMAP passivation layer and the Cu:NiO_x HTL was also probed by XPS measurements. On the survey spectrum (**Fig. S3**), the appearance of the N 1s peak at ca. 400 eV after the passivation unambiguously demonstrates the presence of DMAP on the Cu:NiO_x surface. High-resolution Ni 2p spectra recorded for both passivated and pristine NiO_x films have a broad

multipeak nature due to the complex shake-up losses typical for this transition metal, shown in **Fig. 1D** and **Fig. S4 a/b**. The spectra of both the DMAP-passivated and the non-passivated HTL can be fitted using the same set of peaks without any contributions from Ni^0 and Ni^{3+}.[33] The main Ni 2p3/2 component is situated at 853.55 eV for NiO_x and 853.43 eV for NiO_x /DMAP. As discussed before, the nucleophilic pyridine nitrogen present in DMAP coordinates to Ni^{2+} [34,35] donating electrons and thus inducing the observed 0.12 eV shift of the Ni 2p3/2 peak to lower binding energies for the passivated sample. This electron-donating character of DMAP[36] should also lower the work function (WF) of NiO_x.[37] Concomitantly, the decrease of free carrier (hole) concentration can lead to a reduction of the conductivity of the passivated NiO_x layer.[38] To probe the effects of DMAP passivation on the energy level positions of the HTL, ultraviolet photoelectron spectroscopy (UPS) was performed (cf. **Fig. 1E-F**; full spectra: **Fig. S5**). After DMAP treatment, it can be seen that the WF shifts from –4.71[39] to –4.51 eV. The changed WF of DMAP modified Cu:NiOx results in a larger built-in potential V_{bi} and a wider depletion region. This built-in field can improve the charge separation, charge transport, and the collection of photogenerated carriers, as well as suppress the back transfer of holes from the HTL to the perovskite layer.[40] Besides the shift of WF, the valence band maximum (VBM) of the HTL with DMAP passivation is lowered from –5.0 eV[39] to –5.26 eV (cf. **Fig. S6**), which is beneficial for hole extraction. The energy level scheme of the perovskite solar cell is shown in **Figure S6**. Summarizing, DMAP has not only the role of an anchoring layer for the perovskite on the Cu:NiO_x HTL but also induces a more favorable energy level alignment at the HTL–perovskite interface, which is expected to improve hole extraction.

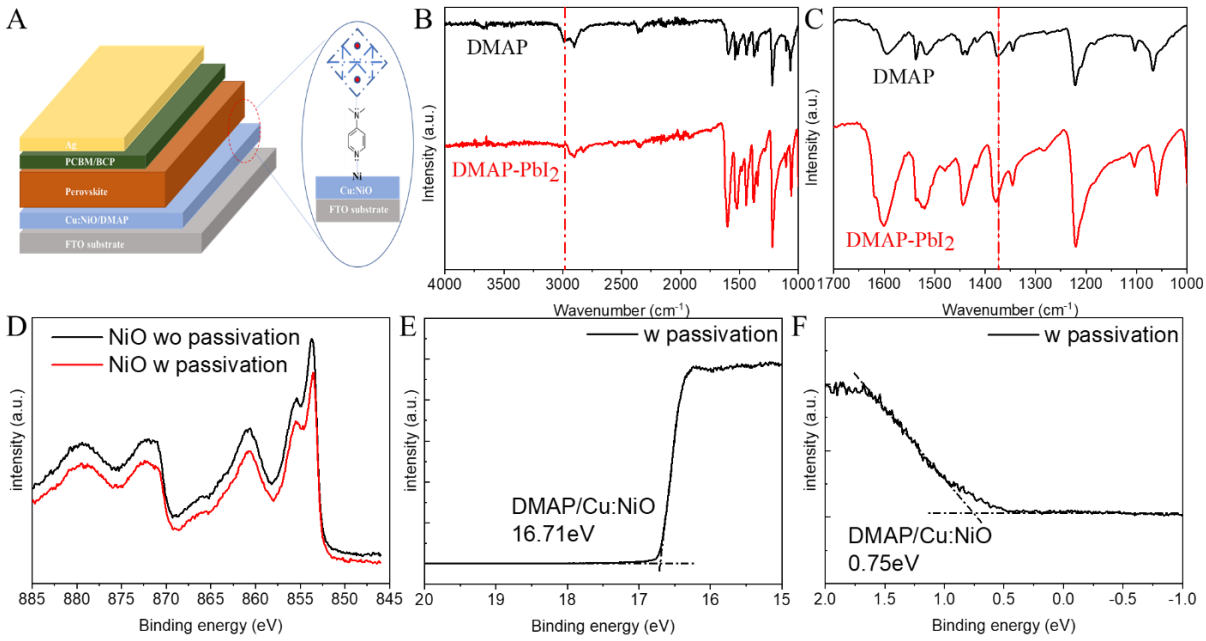

Figure 1: A) Perovskite solar cell architecture used in this work; inset: schematic view of the interaction of DMAP with the HTL and the perovskite. B) FTIR spectra of DMAP and a DMAP-PbI_2 mixture heated to 150 °C for 5 min. C) Enlarged view of the FTIR spectra. D) High-resolution XPS spectra of Ni 2p. E/F) UPS spectra of the Cu:NiO_x HTL with DMAP passivation layer.

After deposition of the CsFAMA triple-cation perovskite, the effect of the presence of DMAP on the crystalline quality of this layer was studied with X-ray diffraction. **Figure 2A** displays the diffractograms obtained for perovskite films grown on bare and on DMAP-passivated Cu:NiO_x HTLs. In both cases, the peak positions are coherent with the diffraction pattern expected for the cubic α-phase (space group $Pm\bar{3}m$) of the triple-cation perovskite with low methylammonium content, adopting essentially the crystal structure of $FAPbI_3$.[41] However, a slight shift of the diffraction peaks to larger angles is observed in the case of the DMAP-passivated sample (**Fig. 2B**), corresponding to a decrease of the lattice parameter from 6.276 ± 0.005 Å to 6.260 ± 0.005 Å. A peak at 44.1° associated with the polycrystalline FTO substrate (ICDD PDF4 #04-008-8130) is visible in both cases, indicating that the X-rays penetrated the entire perovskite layer. Moreover, a peak is present at 14.69° corresponding to the (001) Bragg reflection of hexagonal PbI_2 (ICDD PDF4 #01-079-0803). The relative intensities of the peaks are similar for the two perovskite patterns. Here the ratio between the perovskite phase *(022)* and *(002)* peak intensities is taken as an example. For both the perovskite layer grown on the bare Cu:NiO_x HTL and the DMAP-passivated HTL the ratio is close to 0.06. Therefore, it can be concluded that the

use of DMAP does not change the preferential orientation within the perovskite layer.[42] For a more detailed comparison, the perovskite film microstructure has to be considered, as it can directly affect the performance of the PSC.[43,44] In the present case, it mainly concerns the perpendicular crystallite size and strain (distortion). The configuration used for the XRD measurements was optimized to favor a high diffracted intensity. The counterpart is a non-negligible contribution of the instrumental resolution to the broadening of the Bragg peaks. While a quantitative determination of this contribution is difficult to achieve in a reliable way, qualitative information can be obtained when analyzing the evolution of the full width at half maximum (FWHM) of the peaks as a function of the scattering angle 2θ. From cross-sectional SEM images, the perpendicular crystallite size appears to be larger than 100 nm (shown in **Fig. S7**). Therefore, the peak broadening stems mainly from the presence of distortion in the perovskite lattice. This hypothesis is confirmed by the analysis of the 2θ dependencies of the FWHM values of the (00l) diffraction peaks, as displayed in **Fig. 2C**. If the contribution of the crystallite size were the dominant factor for the observed line broadening, the FWHM values should exhibit a lower increase with 2θ (cf. Supplementary Note 1). As an example, 100-nm sized crystallites would induce a peak broadening of 0.10° and 0.12° at 2θ = 30° and 70°, respectively. Hence, for both types of perovskite layers, the peak broadening mainly arises from the presence of strain. However, there is a distinct difference in the slope of the broadening with increasing 2θ, which is much lower in the case of the sample containing the DMAP-passivated HTL. It can therefore be concluded that DMAP improves the crystalline quality of the perovskite layer by significantly reducing strain.

Since the thicknesses of the perovskite layers based on the two different substrates are nearly the same (around 650 nm, cf. **Fig. S7**), we are able to investigate whether the differences in the perovskite crystallization affect the light-harvesting properties. The comparison of the UV-vis absorption spectra (**Fig. 2D**) shows a slight enhancement of the light absorption in the whole spectral range when DMAP passivation was used. In addition, steady-state photoluminescence (PL) measurements were performed to study the hole extraction efficiency. While both samples exhibit an emission peak centered at 760 nm, the PL intensity of the two stacks differs markedly (**Fig. 2E**). At a first glance, this difference is unexpected when considering that at least 90% of the light should be absorbed in the first 200 nm of the perovskite film and thus should not be directly affected by the interface modification.[1] Moreover, the DMAP-passivated HTL leads to a perovskite layer of better crystalline quality, which should in principle lead to lower quenching due to a decreased trap density. However, the modified HTL has also an

improved interface with the perovskite layer. As a consequence, the observed significant PL quenching behavior indicates that the perovskite film grown on Cu:NiO_x/DMAP enables faster charge transfer kinetics and higher hole extraction ability than that grown on the non-passivated HTL. These features effectively reduce the radiative carrier recombination in the PSC active layer and increase the *FF* of the device.

To learn more about the underlying charge carrier recombination mechanisms, the relationship between the *Voc* of the PSCs and the incident light intensity was examined. If the recombination of free electrons and holes in the active layer dominates, the slope of *Voc* vs. light intensity is larger than kT/q, and *Voc* strongly depends on the incident light intensity (where q is the electron charge, k is the Boltzmann constant, and T is the Kelvin temperature).[42] As visible in **Fig. 2F**, the slope of the stack without the DMAP passivation layer is 2.1 kT/q, whereas that of the stack containing the DMAP layer is significantly lower (1.19 kT/q). This result provides strong evidence that the interfacial barrier for hole extraction is considerably reduced when the DMAP passivation of the HTL is applied. These findings further support the assumption that carrier recombination is largely suppressed by the passivation layer, which can be attributed to a combination of factors including reduced perovskite crystal strain/better perovskite crystalline quality, as well as improved hole extraction due to the modified HTL/perovskite interface.

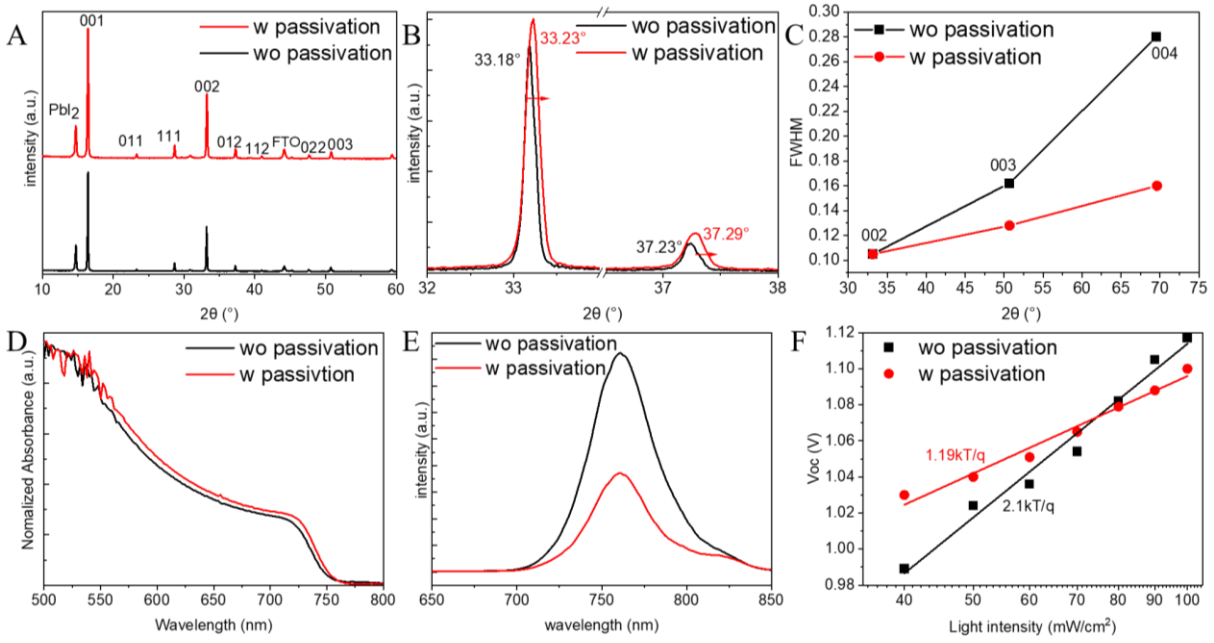

Figure 2: Comparison of the stacks FTO/Cu:NiO_x/DMAP/CsFAMA and FTO/Cu:NiO_x/CsFAMA. A/B) XRD patterns: A) overview, B) enlarged view highlighting the shift of the diffraction peaks to larger angles in the DMAP-containing stack. C) Linewidth (FWHM) of the (00l) perovskite diffraction peaks as a function of 2θ. D) UV–vis absorption spectra. E) Steady-state PL spectra (excited at 400 nm from the perovskite side). F) Device V_{OC} vs. incident light intensity.

Top-view scanning electron microscopy (SEM) images (**Figure 3A**) demonstrate that without DMAP passivation a few holes as well as a large number of small dots are visible on the perovskite surface. According to the literature,[46] the latter can be attributed to excess PbI_2, which appears brighter than the CsFAMA perovskite in the dark-field images due to its higher electron density. In presence of the DMAP passivation layer, the amount of excess PbI_2 on the surface and the number of pinholes reduce significantly (**Fig. 3C**). The surface roughness of the perovskite layers grown on the two types of substrates was investigated with AFM, as illustrated in **Figure 3B/D**. The lateral sizes of the crystallites are around 400 nm on both types of HTL, but perovskite films grown on bare Cu:NiO_x exhibit a higher roughness of 17.3±1.6 nm RMS, compared to those on NiO_x/DMAP (12.4±0.8 nm RMS). Concluding, SEM and AFM analyses demonstrate that the DMAP passivation layer not only induces a favorable perovskite morphology, i.e., a dense film of low surface roughness, but also results in the reduction of the amount of excess PbI_2 on the perovskite layer surface. Due to the high-lying conduction band edge of PbI_2 (3.4eV),[47] its large excess at the perovskite surface generates an energy barrier for charge extraction[48] and decreases the device stability under illumination.[49] Accordingly, it has been reported that only a small amount of unreacted PbI_2 near the perovskite surface is desirable for decreasing recombination processes at the perovskite/charge transport layer interface.[50,51]

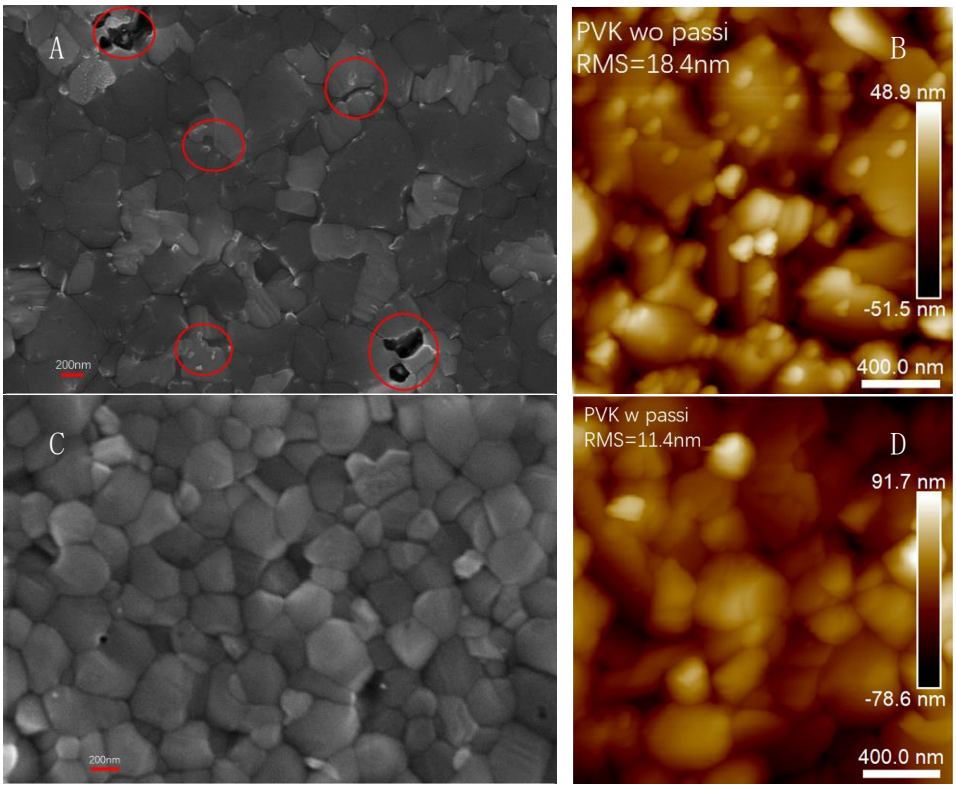

Figure 3: A/C) Top-view SEM and AFM images of the CsFAMA perovskite layer grown on the bare Cu:NiO_x HTL, excess PbI_2 and pinholes are marked with red circles. B/D) Top-view SEM and AFM images of the perovskite grown on DMAP-passivated Cu:NiO_x.

To gain further insight how DMAP affects the PbI_2 distribution within the perovskite layer, grazing incidence X-ray diffraction (GIXRD) was performed. Changing the incident angle ω of the X-ray beam allows for the analysis of the perovskite phase with different penetration depths in the layer. The probed depth h can be determined using the following formula, where D is the penetration depth calculated from the mass absorption coefficient and the density of the material (cf. **Fig. 4A**):

$$sin\omega = \frac{h}{D}$$

Scans varying the scattering angle 2θ were performed at different fixed incident angles ω whose choice determines the depth probed in the sample. **Figure 4B** presents the data obtained for ω values varying from 0.3° to 1.0°, which correspond to probed thicknesses ranging between approximately 40 nm and 200 nm (the full XRD patterns obtained with the different incident angles are shown in **Figure S8**). For all depths probed, the diffraction peaks characteristic of the cubic perovskite phase are present as well as the (001) Bragg peak of PbI_2, while the contribution of FTO is missing as expected. Importantly, for both types of samples (with/without DMAP), the variation of the relative intensities of the PbI_2 and

perovskite contributions with the incident angle show distinct differences. To quantify this evolution, the ratio of the areas of the PbI_2 (001) and α-phase CsFAMA (001) peaks was calculated and its evolution as a function of the probed depth is depicted in **Figure 4C**. It should be noted that the values at 650 nm (entire film thickness) are from the standard θ-2θ WAXS measurement, which accounts for the complete amount of the PbI_2 and perovskite phases in the layer. At this point, the ratio of the peak areas is very similar for the samples with and without DMAP passivation showing that the total amounts of PbI_2 and perovskite in the active layer are essentially the same. Also, for both samples the amount of PbI_2 is maximum in the upper part of the layer, demonstrating that the growth of the perovskite phase is bottom-up, with at least part of the excess lead iodide remaining near the surface. However, the higher ratio value for the non-passivated sample clearly indicates that the amount of untransformed PbI_2 close to the perovskite surface is significantly higher, which was also observed in SEM (**Fig. 3A**). This surface-sensitive XRD technique thus proves that the DMAP passivation layer influences the distribution of PbI_2 throughout the active layer, and promotes the formation of the perovskite phase near the surface. In contrast, as illustrated in **Figure 4D**, for samples without DMAP passivation excess PbI_2 precipitates from perovskite crystals and enriches the surface of the perovskite layer in the process of annealing. After the introduction of the passivation layer, the coordination of DMAP molecules with PbI_2 is supposed to slow down the conversion of PbI_2 to the perovskite at the initial deposition process. Indeed, the nature of the first perovskite plane at the interface with the substrate has been shown to govern the texture and strain of the active layer.[52] A relatively stable, ultrathin PbI_2 layer can ensure the uniform growth of the perovskite layer in the following annealing step and at the same time reduce the enrichment of PbI_2 on the surface of the active layer, which has been shown to decrease the probability of charge recombination at the interface between the perovskite and top charge transport layer (ETL).[53]

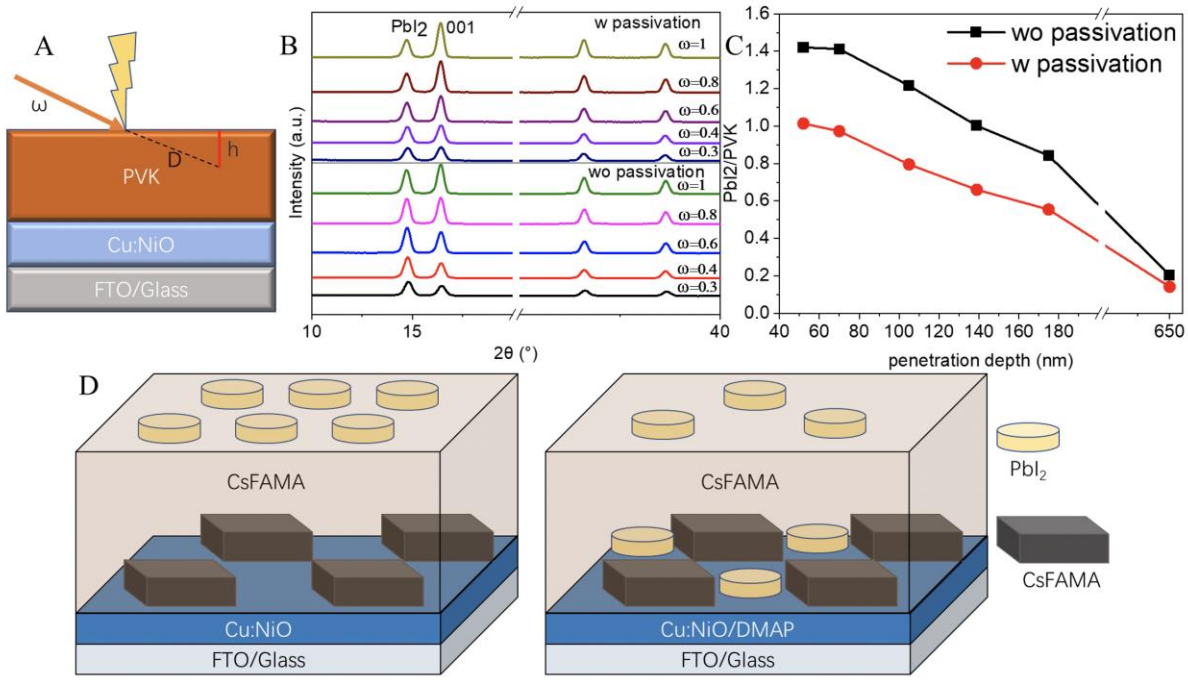

Figure 4: A) Scheme representing the principle of the GIXRD measurements used to probe different depths *h* of the perovskite layer by varying the incident angle ω (*D*: penetration depth, PVK: perovskite). B) XRD patterns obtained for different incident angles. C) Relative intensities of the PbI_2 and α-phase CsFAMA (001) peaks of the samples with/without DMAP passivation of the Cu:NiO_x HTL. D) Schematic illustration of the DMAP-induced differences in the perovskite layer composition near the HTL and near the surface.

Based on the above analyses, the DMAP-modified Cu:NiO_x layer is expected to be beneficial for enhancing the solar cell device performance, due to a better interfacial contact and improved crystalline quality of the perovskite layer. Optimization of the thicknesses of the different layers in our devices using the stack FTO/ Cu:NiO_x/DMAP/CsFAMA/PCBM/BCP/Ag resulted in 40~60 nm for the HTL, around 650 nm for the CsFAMA perovskite, 70 nm for [60]PCBM, 4 nm for BCP and 200 nm for the Ag counter-electrode. The *J–V* curves of the best performing devices are shown in **Figure 5A** and their *J–V* parameters are summarized in **Table 1**. For devices with the passivation layer, the PCE reached values up to 17.90%, i.e., more than 2% higher than the best devices without DMAP (15.73% PCE). **Figures 5B/C** show the statistical distribution of the *PCE* and *FF* measured on 34 devices (comparison of *Voc* and *Jsc* cf. **Figure S9**). **Figure 5C** demonstrates that the devices based on the DMAP-modified Cu:NiO_x layer systematically present a higher *FF*, which is the principal parameter improved by the

passivation even though statistically a small increase of the *Jsc* is also observed. For the cells based on bare Cu:NiO_x layers, the average *FF* lies around 0.63, whereas for devices with the DMAP/ Cu:NiO_x HTL it accounts for 0.75 (highest value: 0.78). These results confirm the advantages of the DMAP passivation discussed before, namely enhanced hole extraction, improved perovskite crystalline quality, and slightly enhanced light-harvesting of the devices. Furthermore, **Figure 5D** shows that the *J–V* hysteresis almost disappeared for the cells containing DMAP, with the hysteresis index decreasing from around 6% to 0.9%. The smaller hysteresis is a further indicator of the better charge extraction induced by the more favorable energy level alignment and less nonradiative recombination at the interface between the perovskite and the HTL.

	***Voc* (V)**	***Jsc* (mA/cm²)**	***FF* (%)**	***PCE (%)***	**Average *PCE* (%)**	**Hysteresis index (%)**
w/o DMAP descending	1.13	20.80	68.93	16.20	15.73	6.04
w/o DMAP ascending	1.10	20.55	67.46	15.25		
w DMAP descending	1.10	20.94	78.46	17.98	17.90	0.90
w DMAP ascending	1.09	20.91	78.22	17.82		

Table 1: Device parameters and hysteresis of the best performing PSCs using DMAP-passivated and non-passivated Cu:NiO_x HTLs. The hysteresis index is calculated as follows:

$$Hysteresis\ \ index = \frac{PCE_{descending} - PCE_{ascending}}{PCE_{average}} * 100\%$$

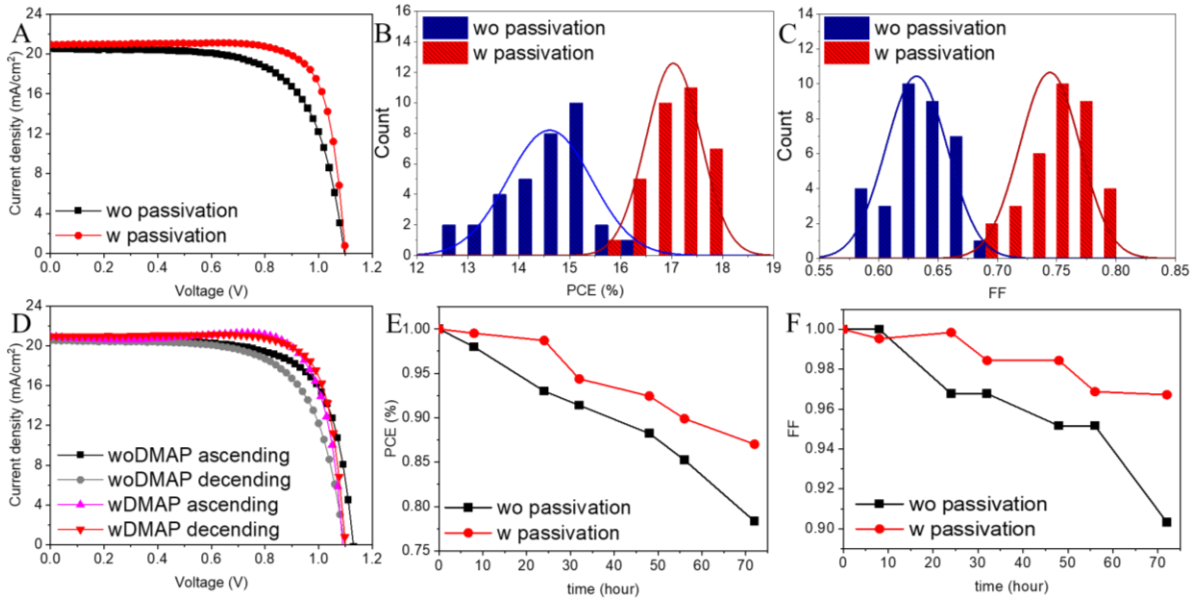

Figure 5: Comparison of the solar cell performances and stability of devices with or without DMAP passivation of the Cu:NiO_x HTL. A) *J–V* curves of the best performing solar cells. B/C) Statistical distribution of the *PCE* and *FF* values obtained from 34 devices of each type. D) *J–V* curves obtained by reverse and forward scans. E/F) Relative evolution of *PCE* and *FF* with the storage time of the non-encapsulated solar cells in the ambient atmosphere (50% humidity).

Finally, we analyzed the stability of both types of devices under ambient air (50% humidity, 25°C) in the dark, which can give a first indication of the environmental robustness of the obtained solar cells. As visible in **Figure 5E**, the DMAP-modified device maintained 87% of its initial PCE after 72h storage, against 77% for the cell without DMAP modification. This difference stems essentially from the *FF* (cf. **Fig. 5F**), which is strongly decreasing with storage time under ambient air when utilizing bare Cu:NiO_x HTLs. We hypothesize that the higher crystalline quality and lower strain of the perovskite layer formed on the passivation layer accounts for the observed enhanced stability. Furthermore, as demonstrated above, the presence of the DMAP passivation layer alters the distribution of lead iodide inside the perovskite crystal, resulting in fewer pinholes and defects, which directly affects the *FF*. Over time, these defects may extend in the cells without DMAP, negatively impacting their performance.[54] Yet another explanation could be related to the removal of impurity ions at the NiO_X surface due to the DMAP passivation, an effect which has been shown to improve the performance of PSCs when treating the HTL with ionic liquids.[55] We underline that the presented stability test aims at the comparison of the behavior of perovskite solar cells fabricated under identical conditions with the only difference being

the DMAP passivation layer. In a more applied perspective, the operational stability of the PSCs could be further strongly enhanced by employing appropriate encapsulation techniques.

3. Conclusions

We demonstrated the beneficial effects of the bifunctional molecule DMAP, used to passivate Cu:NiO_x HTLs, on the performance and stability of planar *p-i-n* perovskite solar cells. DMAP enables the cross-linking between the Cu:NiO_x HTL and the triple-cation (CsFAMA) perovskite via the coordination of the pyridine nitrogen on the metal sites of the Cu:NiO_x HTL and interaction of the remaining dimethylamino function with Pb ions. The use of DMAP results in an improved perovskite crystalline quality with reduced strain, a better perovskite film morphology without pinholes, and a more favorable energy level alignment for hole extraction. These improvements combined with a modified PbI_2 distribution throughout the perovskite layer enhance the charge carrier extraction and transport and reduce undesired charge recombination processes at the interfaces, which in turn results in better solar cell performances. The main factor of improvement was the fill factor, which led to an average increase of the *PCE* by more than 2.2% compared to devices without DMAP up to values close to 18%. Furthermore, the cells with DMAP passivation exhibited strongly reduced hysteresis and improved stability in a high humidity environment. This study contributes to the emerging field of interface engineering of perovskite solar cells by correlating the manifold changes induced by the functionalization of the Cu:NiO_x HTL with the device behavior. In particular, our results demonstrate both the opportunities and challenges related to the functionalization of the substrate used for the growth of the perovskite layer. The quality of the latter is strongly dependent on the precise preparation conditions but the underlying substrate also plays an important role.[56] When novel molecules for the functionalization of the charge transport layers are used, their simultaneous influence on the perovskite nucleation and growth and the interfacial electronic properties are generally difficult to predict, and only very few examples exhibit a synergistic beneficial behavior. Based on the results obtained on Cu:NiO_x HTLs, we expect that DMAP can also be successfully used for the functionalization of other interfaces within perovskite solar cells, in particular those involving metal oxide charge transport layers. Furthermore, the proposed approach could be combined with the latest advances in *p-i-n* PSCs achieved through the engineering of the perovskite/ETL interface via functionalization with organometallic compounds, which led to record efficiency and stability.[13]

4. Experimental section

4.1. Materials:

FTO glass substrates were purchased from Youxuan Technology (6 Ω sq^{-1}). Formamidinium iodide (FAI), methylammonium bromide (MABr), and methylammonium chloride (MACl) were procured from GreatCell Solar. PbI_2 was purchased from Xi'an Polymer Light Technology Corp. Lead (II) bromide ($PbBr_2$, 99%), [6,6]-Phenyl C61 butyric acid methyl ester ([60]PCBM, 99%), Bathocuproine (BCP, 99%), chlorobenzene (anhydrous, 99.8%), dimethylsulfoxide (DMSO, anhydrous, ≥99.9%), N, N-dimethylformamide (DMF, anhydrous, 99.8%), monoethanolamine ($NH_2CH_2CH_2OH$, MEA), 4-dimethylaminopyridine (DMAP, 99%) and isopropyl alcohol (IPA, anhydrous, 99.5%) were purchased from Sigma Aldrich. Nickel acetate tetrahydrate ($Ni(CH_3COO)_2{\cdot}4H_2O$) and copper(II) acetate monohydrate ($Cu(CH_3COO)_2{\cdot}H_2O$) were acquired from Alfa Aesar. All chemicals were used without further purification.

4.2. NiO_x precursor solution:

Nickel acetate tetrahydrate ($Ni(CH_3COO)_2{\cdot}4H_2O$) and Copper(II) acetate monohydrate ($Cu(CH_3COO)_2{\cdot}H_2O$) (mole radio Cu/Ni = 5%) were dissolved in ethanol with monoethanolamide ($NH_2CH_2CH_2OH$) (0.2 mol L^{-1}). The mole ratio of metal ions: MEA was maintained at 1:1 in solution. The dissolution took place while stirring in a sealed glass vial under air at 40° C for 1 h. The solution appeared homogeneous and deep green after approximately 40 min.

4.3. Device Fabrication:

FTO-coated glass substrates were sequentially cleaned in acetone, detergent solution, deionized water, and isopropyl alcohol baths for 30 min each. Then, the substrates were exposed to UV–ozone for 45 min to remove residual organic pollutants. The Cu:NiO_x precursor was deposited by spin-casting onto the FTO substrates (70 μL solution, acceleration 3000 rpm/s, speed 3000 rpm, duration 30 s). Unless otherwise stated, the Cu:NiO_x precursor films were heated to 275 °C for 45 min in air, then the temperature was raised to 500°C for 60 min in air. For surface modification, a DMAP solution in IPA with the concentration of 20 mg/mL, was spin-coated (70 μL solution using the same spinning

parameters) onto the as-prepared Cu:NiO_x films. Then the substrates were annealed on a hotplate at 100°C for 5 min inside an Ar-filled glovebox.

For the deposition of the perovskite films, we followed the procedure reported in our previous work.[57] Briefly, a precursor solution was prepared by mixing PbI_2 (1.45 M), FAI (1.15 M), $PbBr_2$ (0.21 M), MABr (0.21 M), and MACl (0.45 M) in 1 mL of a mixed solvent of DMF/DMSO (4:1 v/v). Then, 17.5 μL of CsI solution (2 M in DMSO) was added to form the triple cation (Cs/MA/FA) perovskite. Next, the obtained solution was deposited onto the HTL substrates by two consecutive spin-coating steps, at 1000 and 4000 rpm for 10 and 25 s, respectively. During the second spin-coating step, 150 μL of chlorobenzene was dropped onto the substrate after 15 s. Then, the substrate was immediately moved to a hotplate and annealed at 100°C for 50 min. After cooling down to room temperature, 60 μL of a 20×10^{-3} M [60]PCBM solution in CB was spin-coated onto the perovskite surface at a spinning rate of 1500 rpm for 45 s followed by spin-coating of a BCP solution (1mg/mL in IPA solution, 4000 rpm, 30 s). To complete the device, 200 nm thick Ag electrodes were deposited on top by thermal evaporation. The electrode area is 0.909 cm^2

4.4. Characterization:

A Zeiss Ultra 55 high-resolution scanning electron microscope was used to examine the morphology of the films and acquire cross-sectional images of the entire device. A Panalytical Empyrean diffractometer with a cobalt anode (Co Kα1 = 1.7890, Co Kα2 = 1.7929), a Göbel mirror, and a 1D Pixcel detector were used to perform XRD analyses. The UV-vis absorption spectra were measured using a Shimadzu UV-1800 spectrometer. Current-voltage measurements of the devices were performed with a Keithley 2400 Source meter under AM 1.5G illumination with a xenon-lamp-based calibrated solar simulator (Newport, AAA) with 100 mW/cm² intensity unless stated otherwise. The cells were measured with a mask (0.09 cm^2) and the scan rate was 20 mV • s^{-1} for both forward and reverse scans. AFM images were acquired with a Bruker Dimension Icon atomic force microscope. Photoluminescence spectra were recorded using a FLUOROLOG-3 spectrophotometer (Jobin-Yvon). The UPS measurements for all samples were performed on an M-XPS spectrometer from Omicron Nanotechnology equipped with a monochromated Al Kα source (hν=1486.6 eV) and an ultraviolet He lamp (He I=21.2 eV). Photoelectrons were collected under normal geometry by a hemispherical analyzer,

with an angular acceptance of 8°. XPS analyses were carried out with a Versa Probe II spectrometer (ULVAC-PHI) equipped with a monochromated Al Ka source (hν = 1486.6 eV). The core-level peaks were recorded with a constant pass energy of 23.3 eV. The XPS spectra were fitted with CasaXPS software using Shirley background and a combination of Gaussian (70%) and Lorentzian (30%) distributions. Binding energies were referenced with respect to adventitious carbon (C 1s BE = 284.8 eV).

Supporting Information

XPS and UPS spectra and data, energy level scheme and cross-sectional SEM images of the devices, full-range GIXRD patterns, statistical distribution of the solar cell parameters, photographs of DMAP and PbI_2 powders and their mixture after heating to 150°C.

Acknowledgment

The authors acknowledge the French Research Agency ANR for financial support (Grant PERSIL ANR-16-CE05-0019-02), and the LABEX Lanef (ANR-10-LABX-51-01) for its support with mutualized instrumentation. Part of this work was realized on the SyMMES' Hybrid-En facility, and Etienne Omnès is thanked for experimental support. The PhD thesis of Yuze Li is funded by UGA IDEX (project IRS C-Super), which is gratefully acknowledged.

Present address: Key Laboratory of Photovoltaic and Energy Conservation Materials, Institute of Solid-State Physics, Hefei Institutes of Physical Science, Chinese Academy of Sciences, Hefei 230031, China

References

(1) De Wolf, S.; Holovsky, J.; Moon, S. J.; Löper, P.; Niesen, B.; Ledinsky, M.; Haug, F. J.; Yum, J. H.; Ballif, C. Organometallic Halide Perovskites: Sharp Optical Absorption Edge and Its Relation to Photovoltaic Performance. *J. Phys. Chem. Lett.* **2014**, *5* (6), 1035–1039. https://doi.org/10.1021/jz500279b.

(2) Adhyaksa, G. W. P.; Veldhuizen, L. W.; Kuang, Y.; Brittman, S.; Schropp, R. E. I.; Garnett, E. C. Carrier Diffusion Lengths in Hybrid Perovskites: Processing, Composition, Aging, and Surface Passivation Effects. *Chem. Mater.* **2016**, *28* (15), 5259–5263.

https://doi.org/10.1021/acs.chemmater.6b00466.

(3) Kim, H. S.; Lee, C. R.; Im, J. H.; Lee, K. B.; Moehl, T.; Marchioro, A.; Moon, S. J.; Humphry-Baker, R.; Yum, J. H.; Moser, J. E.; Grätzel, M.; Park, N. G. Lead Iodide Perovskite Sensitized All-Solid-State Submicron Thin Film Mesoscopic Solar Cell with Efficiency Exceeding 9%. *Sci. Rep.* **2012**, *2*, 1–7. https://doi.org/10.1038/srep00591.

(4) Jeong, M.; Choi, I. W.; Go, E. M.; Cho, Y.; Kim, M.; Lee, B.; Jeong, S.; Jo, Y.; Choi, H. W.; Lee, J.; Bae, J. H.; Kwak, S. K.; Kim, D. S.; Yang, C. Stable Perovskite Solar Cells with Efficiency Exceeding 24.8% and 0.3-V Voltage Loss. *Science (80-.).* **2020**, *369* (6511), 1615–1620. https://doi.org/10.1126/science.abb7167.

(5) Tavakoli, M. M.; Yadav, P.; Tavakoli, R.; Kong, J. Surface Engineering of TiO2 ETL for Highly Efficient and Hysteresis-Less Planar Perovskite Solar Cell (21.4%) with Enhanced Open-Circuit Voltage and Stability. *Adv. Energy Mater.* **2018**, *8* (23), 1–9. https://doi.org/10.1002/aenm.201800794.

(6) Kim, H. S.; Mora-Sero, I.; Gonzalez-Pedro, V.; Fabregat-Santiago, F.; Juarez-Perez, E. J.; Park, N. G.; Bisquert, J. Mechanism of Carrier Accumulation in Perovskite Thin-Absorber Solar Cells. *Nat. Commun.* **2013**, *4*, 1–7. https://doi.org/10.1038/ncomms3242.

(7) Van Reenen, S.; Kemerink, M.; Snaith, H. J. Modeling Anomalous Hysteresis in Perovskite Solar Cells. *J. Phys. Chem. Lett.* **2015**, *6* (19), 3808–3814. https://doi.org/10.1021/acs.jpclett.5b01645.

(8) Stoumpos, C. C.; Malliakas, C. D.; Kanatzidis, M. G. Semiconducting Tin and Lead Iodide Perovskites with Organic Cations: Phase Transitions, High Mobilities, and near-Infrared Photoluminescent Properties. *Inorg. Chem.* **2013**, *52* (15), 9019–9038. https://doi.org/10.1021/ic401215x.

(9) Huang, D.; Goh, T.; McMillon-Brown, L.; Kong, J.; Zheng, Y.; Zhao, J.; Li, Y.; Zhao, S.; Xu, Z.; Taylor, A. D. PEOz-PEDOT:PSS Composite Layer: A Route to Suppressed Hysteresis and Enhanced Open-Circuit Voltage in a Planar Perovskite Solar Cell. *ACS Appl. Mater. Interfaces* **2018**, *10* (30), 25329–25336. https://doi.org/10.1021/acsami.8b05949.

(10) Bi, C.; Wang, Q.; Shao, Y.; Yuan, Y.; Xiao, Z.; Huang, J. Non-Wetting Surface-Driven High-Aspect-Ratio Crystalline Grain Growth for Efficient Hybrid Perovskite Solar Cells. *Nat. Commun.* **2015**, *6*, 1–7. https://doi.org/10.1038/ncomms8747.

(11) Luo, D.; Yang, W.; Wang, Z.; Sadhanala, A.; Hu, Q.; Su, R.; Shivanna, R.; Trindade, G. F.; Watts,

J. F.; Xu, Z.; Liu, T.; Chen, K.; Ye, F.; Wu, P.; Zhao, L.; Wu, J.; Tu, Y.; Zhang, Y.; Yang, X.; Zhang, W.; Friend, R. H.; Gong, Q.; Snaith, H. J.; Zhu, R. Enhanced Photovoltage for Inverted Planar Heterojunction Perovskite Solar Cells. *Science (80-.).* **2018**, *360* (6396), 1442–1446. https://doi.org/10.1126/science.aap9282.

(12) Teddy Salim, Shuangyong Sun, Yuichiro Abe, Anurag Krishna, A. C. G. and Y. M. L. Perovskite-Based Solar Cells: Impact of Morphology and Device Architecture on Device Performance. *J. Mater. Chem. A* **2015**. https://doi.org/10.1039/C5TA00355E.

(13) Li, Z.; Li, B.; Wu, X.; Sheppard, S. A.; Zhang, S.; Gao, D.; Long, N. J.; Zhu, Z. Organometallic-Functionalized Interfaces for Highly Efficient Inverted Perovskite Solar Cells. *Science* **2022**, *376* (6591), 416–420. https://doi.org/10.1126/science.abm8566.

(14) Wang, K. C.; Jeng, J. Y.; Shen, P. S.; Chang, Y. C.; Diau, E. W. G.; Tsai, C. H.; Chao, T. Y.; Hsu, H. C.; Lin, P. Y.; Chen, P.; Guo, T. F.; Wen, T. C. P-Type Mesoscopic Nickel Oxide/Organometallic Perovskite Heterojunction Solar Cells. *Sci. Rep.* **2014**, *4*, 1–8. https://doi.org/10.1038/srep04756.

(15) Chan, I. M.; Hsu, T. Y.; Hong, F. C. Enhanced Hole Injections in Organic Light-Emitting Devices by Depositing Nickel Oxide on Indium Tin Oxide Anode. *Appl. Phys. Lett.* **2002**, *81* (10), 1899–1901. https://doi.org/10.1063/1.1505112.

(16) Manders, J. R.; Tsang, S.; Hartel, M. J.; Lai, T.; Chen, S.; Amb, C. M.; Reynolds, J. R.; So, F. Solution-Processed Nickel Oxide Hole Transport Layers in High Effi Ciency Polymer Photovoltaic Cells. *Adv. Funct. Mater.* **2013**, *23* (23), 2993–3001. https://doi.org/10.1002/adfm.201202269.

(17) Park, J. H.; Seo, J.; Park, S.; Shin, S. S.; Kim, Y. C.; Jeon, N. J.; Shin, H.-W. W.; Ahn, T. K.; Noh, J. H.; Yoon, S. C.; Hwang, C. S.; Seok, S. Il. Efficient CH3NH3PbI3 Perovskite Solar Cells Employing Nanostructured P-Type NiO Electrode Formed by a Pulsed Laser Deposition. *Adv. Mater.* **2015**, *27* (27), 4013–4019. https://doi.org/10.1002/adma.201500523.

(18) Kim, J. H.; Liang, P.; Williams, S. T.; Cho, N.; Chueh, C.; Glaz, M. S.; Ginger, D. S.; Jen, A. K.-Y. High-Performance and Environmentally Stable Planar Heterojunction Perovskite Solar Cells Based on a Solution-Processed Copper-Doped Nickel Oxide Hole-Transporting Layer. *Adv. Mater.* **2015**, *27*, 695–701. https://doi.org/10.1002/adma.201404189.

(19) Li, G.; Jiang, Y.; Deng, S.; Tam, A.; Xu, P.; Wong, M.; Kwok, H. S. Overcoming the Limitations

of Sputtered Nickel Oxide for High-Efficiency and Large-Area Perovskite Solar Cells. *Adv. Sci.* **2017**, *4* (12), 1–8. https://doi.org/10.1002/advs.201700463.

(20) Ru, P.; Bi, E.; Zhang, Y.; Wang, Y.; Kong, W.; Sha, Y.; Tang, W.; Zhang, P.; Wu, Y.; Chen, W.; Yang, X.; Chen, H.; Han, L. High Electron Affinity Enables Fast Hole Extraction for Efficient Flexible Inverted Perovskite Solar Cells. *Adv. Energy Mater.* **2020**, *10* (12), 1–9. https://doi.org/10.1002/aenm.201903487.

(21) Bai, Y.; Chen, H.; Xiao, S.; Xue, Q.; Zhang, T.; Zhu, Z.; Li, Q.; Hu, C.; Yang, Y.; Hu, Z.; Huang, F.; Wong, K. S.; Yip, H. L.; Yang, S. Effects of a Molecular Monolayer Modification of NiO Nanocrystal Layer Surfaces on Perovskite Crystallization and Interface Contact toward Faster Hole Extraction and Higher Photovoltaic Performance. *Adv. Funct. Mater.* **2016**, *26* (17), 2950–2958. https://doi.org/10.1002/adfm.201505215.

(22) Xu, L.; Chen, X.; Jin, J.; Liu, W.; Dong, B.; Bai, X.; Song, H.; Reiss, P. Inverted Perovskite Solar Cells Employing Doped NiO Hole Transport Layers: A Review. *Nano Energy* **2019**, *63*, 103860. https://doi.org/10.1016/j.nanoen.2019.103860.

(23) Zhang, J.; Luo, H.; Xie, W.; Lin, X.; Hou, X.; Zhou, J.; Huang, S.; Ou-Yang, W.; Sun, Z.; Chen, X. Efficient and Ultraviolet Durable Planar Perovskite Solar Cells: Via a Ferrocenecarboxylic Acid Modified Nickel Oxide Hole Transport Layer. *Nanoscale* **2018**, *10* (12), 5617–5625. https://doi.org/10.1039/c7nr08750k.

(24) Li, L.; Wang, Y.; Wang, X.; Lin, R.; Luo, X.; Liu, Z.; Zhou, K.; Xiong, S.; Bao, Q.; Chen, G.; Tian, Y.; Deng, Y.; Xiao, K.; Wu, J.; Saidaminov, M. I.; Lin, H.; Ma, C.-Q.; Zhao, Z.; Wu, Y.; Zhang, L.; Tan, H., Flexible all-perovskite tandem solar cells approaching 25% efficiency with molecule-bridged hole-selective contact. *Nature Energy* **2022,** *7* (8), 708-717. https://doi.org/10.1038/s41560-022-01045-2.

(25) Huang, D.; Xiang, H.; Ran, R.; Wang, W.; Zhou, W.; Shao, Z., Recent Advances in Nanostructured Inorganic Hole-Transporting Materials for Perovskite Solar Cells. *Nanomaterials* **2022,** *12* (15), 2592. https://doi.org/10.1016/j.mtnano.2022.100252.

(26) Zhu, K.; Chen, Y.; Wang, Y.; Feng, M.; Zhao, Y., Progress of solution-processed metal oxides as charge transport layers towards efficient and stable perovskite solar cells and modules. *Materials Today Nano* **2022,** *20*, 100252. https://doi.org/10.1016/j.mtnano.2022.100252.

(27) Zhao, L.; Su, G.; Liu, W.; Cao, L.; Wang, J.; Dong, Z.; Song, M. Optical and Electrochemical

Properties of Cu-Doped NiO Films Prepared by Electrochemical Deposition. *Appl. Surf. Sci.* **2011**, *257* (9), 3974–3979. https://doi.org/10.1016/j.apsusc.2010.11.160.

(28) Barlow, B. C.; Burgess, I. J. Electrochemical Evaluation of 4-(Dimethylamino)Pyridine Adsorption on Polycrystalline Gold. *Langmuir* **2007**, *23* (3), 1555–1563. https://doi.org/10.1021/la0626860.

(29) Sundaraganesan, N.; Kalaichelvan, S.; Meganathan, C.; Joshua, B. D.; Cornard, J. FT-IR, FT-Raman Spectra and Ab Initio HF and DFT Calculations of 4-N,N′-Dimethylamino Pyridine. *Spectrochim. Acta - Part A Mol. Biomol. Spectrosc.* **2008**, *71* (3), 898–906. https://doi.org/10.1016/j.saa.2008.02.016.

(30) Hamill, J. C.; Schwartz, J.; Loo, Y. L. Influence of Solvent Coordination on Hybrid Organic-Inorganic Perovskite Formation. *ACS Energy Lett.* **2018**, *3* (1), 92–97. https://doi.org/10.1021/acsenergylett.7b01057.

(31) Rahimnejad, S.; Kovalenko, A.; Forés, S. M.; Aranda, C.; Guerrero, A. Coordination Chemistry Dictates the Structural Defects in Lead Halide Perovskites. *ChemPhysChem* **2016**, 2795–2798. https://doi.org/10.1002/cphc.201600575.

(32) Stewart, R. J.; Grieco, C.; Larsen, A. V.; Doucette, G. S.; Asbury, J. B. Molecular Origins of Defects in Organohalide Perovskites and Their Influence on Charge Carrier Dynamics. *J. Phys. Chem. C* **2016**, *120* (23), 12392–12402. https://doi.org/10.1021/acs.jpcc.6b03472.

(33) Biesinger, M. C.; Payne, B. P.; Lau, L. W. M.; St, R.; Smart, C. X-Ray Photoelectron Spectroscopic Chemical State Quantification of Mixed Nickel Metal , Oxide and Hydroxide Systems. *Surf. Interface Anal. An Int. J. devoted to Dev. Appl. Tech. Anal. surfaces, interfaces thin Film.* **2009**, No. January, 324–332. https://doi.org/10.1002/sia.3026.

(34) Hercules, D. M. Electron Spectroscopy for Chemical Analysis. *Proc. Soc. Anal. Chem.* **1973**, *10* (12), 193–194. https://doi.org/10.1007/978-1-4684-2961-9_33.

(35) Grim, S. O.; Matienzo, L. J.; Swartz, W. E. X-Ray Photoelectron Spectroscopy of Some Nickel Dithiolate Complexes. *J. Am. Chem. Soc.* **1972**, *94* (14), 5116–5117. https://doi.org/10.1021/ja00769a073.

(36) Garnier, J.; Kennedy, A. R.; Berlouis, L. E. A.; Turner, A. T.; Murphy, J. A. Structure and Reactivity in Neutral Organic Electron Donors Derived from 4-Dimethylaminopyridine. *Beilstein J. Org. Chem.* **2010**, *6*, 4–11. https://doi.org/10.3762/bjoc.6.73.

(37) Lindell, L.; De Jong, M. P.; Osikowicz, W.; Lazzaroni, R.; Berggren, M.; Salaneck, W. R.; Crispin, X. Characterization of the Interface Dipole at the Paraphenylenediamine-Nickel Interface: A Joint Theoretical and Experimental Study. *J. Chem. Phys.* **2005**, *122* (8). https://doi.org/10.1063/1.1851507.

(38) Qiu, Z.; Gong, H.; Zheng, G.; Yuan, S.; Zhang, H.; Zhu, X.; Zhou, H.; Cao, B. Enhanced Physical Properties of Pulsed Laser Deposited NiO Films via Annealing and Lithium Doping for Improving Perovskite Solar Cell Efficiency. *J. Mater. Chem. C* **2017**, *5* (28), 7084–7094. https://doi.org/10.1039/c7tc01224a.

(39) Lee, H.; Yang, W.; Tan, J.; Oh, Y.; Park, J.; Moon, J., Cu-Doped NiOx as an Effective Hole-Selective Layer for a High-Performance Sb2Se3 Photocathode for Photoelectrochemical Water Splitting. *ACS Energy Letters* **2019,** *4* (5), 995-1003. https://doi.org/10.1021/acsenergylett.9b00414

(40) Yang, G.; Wang, C.; Lei, H.; Zheng, X.; Qin, P.; Xiong, L.; Zhao, X.; Yan, Y.; Fang, G. Interface Engineering in Planar Perovskite Solar Cells: Energy Level Alignment, Perovskite Morphology Control and High Performance Achievement. *J. Mater. Chem. A* **2017**, *5* (4), 1658–1666. https://doi.org/10.1039/c6ta08783c.

(41) Zheng, G.; Zhu, C.; Ma, J.; Zhang, X.; Tang, G.; Li, R.; Chen, Y.; Li, L.; Hu, J.; Hong, J.; Chen, Q.; Gao, X.; Zhou, H. Manipulation of Facet Orientation in Hybrid Perovskite Polycrystalline Films by Cation Cascade. *Nat. Commun.* **2018**, *9* (1), 1–11. https://doi.org/10.1038/s41467-018-05076-w.

(42) Bouchard, M.; Hilhorst, J.; Pouget, S.; Alam, F.; Mendez, M.; Djurado, D.; Aldakov, D.; Schülli, T.; Reiss, P. Direct Evidence of Chlorine-Induced Preferential Crystalline Orientation in Methylammonium Lead Iodide Perovskites Grown on TiO2. *J. Phys. Chem. C* **2017**, *121* (14), 7596–7602. https://doi.org/10.1021/acs.jpcc.6b11529.

(43) Zou, Y.; Wang, H. Y.; Qin, Y.; Mu, C.; Li, Q.; Xu, D.; Zhang, J. P. Reduced Defects of MAPbI 3 Thin Films Treated by FAI for High-Performance Planar Perovskite Solar Cells. *Adv. Funct. Mater.* **2019**, *29* (7), 1–7. https://doi.org/10.1002/adfm.201805810.

(44) Medjahed, A. A.; Dally, P.; Zhou, T.; Lemaitre, N.; Djurado, D.; Reiss, P.; Pouget, S. Unraveling the Formation Mechanism and Ferroelastic Behavior of MAPbI3 Perovskite Thin Films Prepared in the Presence of Chloride. *Chem. Mater.* **2020**, *32* (8), 3346–3357.

https://doi.org/10.1021/acs.chemmater.9b04239.

(45) Jiang, Q.; Zhao, Y.; Zhang, X.; Yang, X.; Chen, Y.; Chu, Z.; Ye, Q.; Li, X.; Yin, Z.; You, J. Surface Passivation of Perovskite Film for Efficient Solar Cells. *Nat. Photonics* **2019**, *13* (7), 460–466. https://doi.org/10.1038/s41566-019-0398-2.

(46) Jiang, Q.; Chu, Z.; Wang, P.; Yang, X.; Liu, H.; Wang, Y.; Yin, Z.; Wu, J.; Zhang, X.; You, J. Planar-Structure Perovskite Solar Cells with Efficiency beyond 21%. *Adv. Mater.* **2017**, *29* (46), 1–7. https://doi.org/10.1002/adma.201703852.

(47) Cho, K. T.; Paek, S.; Grancini, G.; Roldán-Carmona, C.; Gao, P.; Lee, Y.; Nazeeruddin, M. K. Highly Efficient Perovskite Solar Cells with a Compositionally Engineered Perovskite/Hole Transporting Material Interface. *Energy Environ. Sci.* **2017**, *10* (2), 621–627. https://doi.org/10.1039/c6ee03182j.

(48) Bi, D.; El-Zohry, A. M.; Hagfeldt, A.; Boschloo, G. Unraveling the Effect of PbI2 Concentration on Charge Recombination Kinetics in Perovskite Solar Cells. *ACS Photonics* **2015**, *2* (5), 589–594. https://doi.org/10.1021/ph500255t.

(49) Schoonman, J. Organic-Inorganic Lead Halide Perovskite Solar Cell Materials: A Possible Stability Problem. *Chem. Phys. Lett.* **2015**, *619*, 193–195. https://doi.org/10.1016/j.cplett.2014.11.063.

(50) Liu, F.; Dong, Q.; Wong, M. K.; Djurišić, A. B.; Ng, A.; Ren, Z.; Shen, Q.; Surya, C.; Chan, W. K.; Wang, J.; Ng, A. M. C.; Liao, C.; Li, H.; Shih, K.; Wei, C.; Su, H.; Dai, J. Is Excess PbI2 Beneficial for Perovskite Solar Cell Performance? *Adv. Energy Mater.* **2016**, *6* (7), 1–9. https://doi.org/10.1002/aenm.201502206.

(51) Merdasa, A.; Kiligaridis, A.; Rehermann, C.; Abdi-Jalebi, M.; Stöber, J.; Louis, B.; Gerhard, M.; Stranks, S. D.; Unger, E. L.; Scheblykin, I. G. Impact of Excess Lead Iodide on the Recombination Kinetics in Metal Halide Perovskites. *ACS Energy Lett.* **2019**, *4* (6), 1370–1378. https://doi.org/10.1021/acsenergylett.9b00774.

(52) Medjahed, A. A.; Zhou, T.; Alvarez Quiceno, J. C.; Dally, P.; Pochet, P.; Schülli, T. U.; Djurado, D.; Reiss, P.; Pouget, S. Microstructure of Methylammonium Lead Iodide Perovskite Thin Films: A Comprehensive Study of the Strain and Texture. *Adv. Energy Mater.* **2022**, *2103627*, 2103627. https://doi.org/10.1002/aenm.202103627.

(53) Wolff, C. M.; Caprioglio, P.; Stolterfoht, M.; Neher, D., Nonradiative Recombination in Perovskite Solar Cells: The Role of Interfaces. *Adv. Mater*. **2019,** *31* (52), 1902762. https://doi.org/10.1002/adma.201902762

(54) Sherkar, T. S.; Momblona, C.; Gil-Escrig, L.; Ávila, J.; Sessolo, M.; Bolink, H. J.; Koster, L. J. A. Recombination in Perovskite Solar Cells: Significance of Grain Boundaries, Interface Traps, and Defect Ions. *ACS Energy Lett.* **2017**, *2* (5), 1214–1222. https://doi.org/10.1021/acsenergylett.7b00236.

(55) Wang, S.; Li, Y.; Yang, J.; Wang, T.; Yang, B.; Cao, Q.; Pu, X.; Etgar, L.; Han, J.; Zhao, J.; Li, X.; Hagfeldt, A., Critical Role of Removing Impurities in Nickel Oxide on High-Efficiency and Long-Term Stability of Inverted Perovskite Solar Cells. *Angew. Chem. Int. Ed.* **2022,** *61* (18), e202116534. https://doi.org/10.1002/anie.202116534

(56) Dunlap-Shohl, W. A.; Zhou, Y.; Padture, N. P.; Mitzi, D. B. Synthetic Approaches for Halide Perovskite Thin Films. *Chem. Rev.* **2019**, *119* (5), 3193–3295. https://doi.org/10.1021/acs.chemrev.8b00318.

(57) Ye, J.; Li, Y.; Medjahed, A. A.; Pouget, S.; Aldakov, D.; Liu, Y.; Reiss, P. Doped Bilayer Tin(IV) Oxide Electron Transport Layer for High Open-Circuit Voltage Planar Perovskite Solar Cells with Reduced Hysteresis. *Small* **2021**, *17* (5), 2005671. https://doi.org/10.1002/smll.202005671.

TOC Graphic:

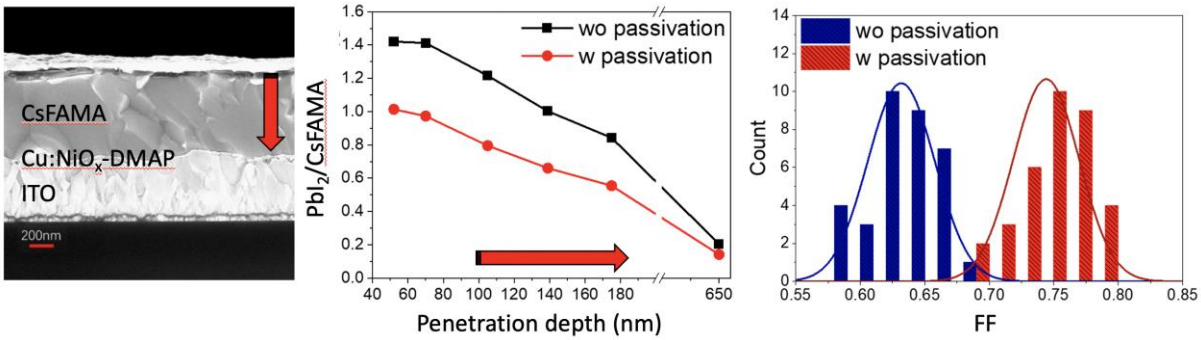
CsFAMA
Cu:NiOx-DMAP
ITO
200nm
wo passivation
w passivation
PbI2/CsFAMA
Penetration depth (nm)
wo passivation
w passivation
Count
FF